

Article

Visible Light-Driven H₂O₂ Photoelectrocatalytic Synthesis Over a Tandem Electrode Strategy

Chao Chen ^{1,2}, Nakata Takumu ¹, Wenan Cai ¹, Qitao Zhang ^{2,*} and Teruhisa Ohno ^{1,*}

¹ Department of Applied Chemistry, Faculty of Engineering, Kyushu Institute of Technology, 1-1 Sensuicho, Tobata, Kitakyushu 804-8550, Japan; chenchao@szu.edu.cn (C.C.); nakata.takumu288@mail.kyutech.jp (N.T.); cai.wen-an679@mail.kyutech.jp (W.C.)

² International Collaborative Laboratory of 2D Materials for Optoelectronics Science and Technology of Ministry of Education, Institute of Microscale Optoelectronics, Shenzhen University, Shenzhen 518000, China

* Corresponding authors: qitao-zhang@szu.edu.cn (Q.Z.); tohno@che.kyutech.ac.jp (T.O.)

Received: 8 February 2024; Accepted: 16 April 2024; Available online: 23 April 2024

ABSTRACT: Photocatalytic synthesis of hydrogen peroxide (H₂O₂) can be an environmentally friendly and energy-saving solution. However, the oxygen reduction reaction (ORR) rate is limited due to the low solubility of O₂ in water. In this study, a modified BiVO₄ (BVO) photoanode combined with an Sn-coordinated phthalocyanine gas diffusion electrode (SnPc-GDE) was employed for the synthesis of H₂O₂, and the oxygen reduction reaction rate was increased through a unique three-phase interface system. When visible light was irradiated on the BVO photoanode, the hole-electron pairs were excited and the oxygen evolution reaction (OER) was driven through the holes, and the excited electrons were transferred to the SnPc-GDE to reduce O₂ for the synthesis of H₂O₂. Oxygen vacancy enrichment on the BVO electrode was achieved by photoetching and annealing under an N₂ atmosphere, which effectively improved the carrier separation efficiency. Complexation with a WO₃ layer formed a built-in electric field, which further promoted the electron-hole pair separation. The SnPc catalyst-modified GDE electrode has the best selectivity for ORR and remains stable during long-term reactions. Under bias-free conditions, the generation rate of H₂O₂ reached 952.5 μM·L⁻¹·h⁻¹, with a Faradaic efficiency of 48.4%. This study provided a practical strategy for designing a highly efficient BVO/SnPc-GDE photoelectrochemical system to produce H₂O₂ based on improvement in electron-hole transmission efficiency and product selectivity.

Keywords: BiVO₄; Oxygen vacancy; Gas diffusion electrode; O₂ reduction reaction; H₂O₂ production



© 2024 by the authors; licensee SCIEPublish, SCISCAN co. Ltd. This article is an open access article distributed under the CC BY license (<http://creativecommons.org/licenses/by/4.0/>).

1. Introduction

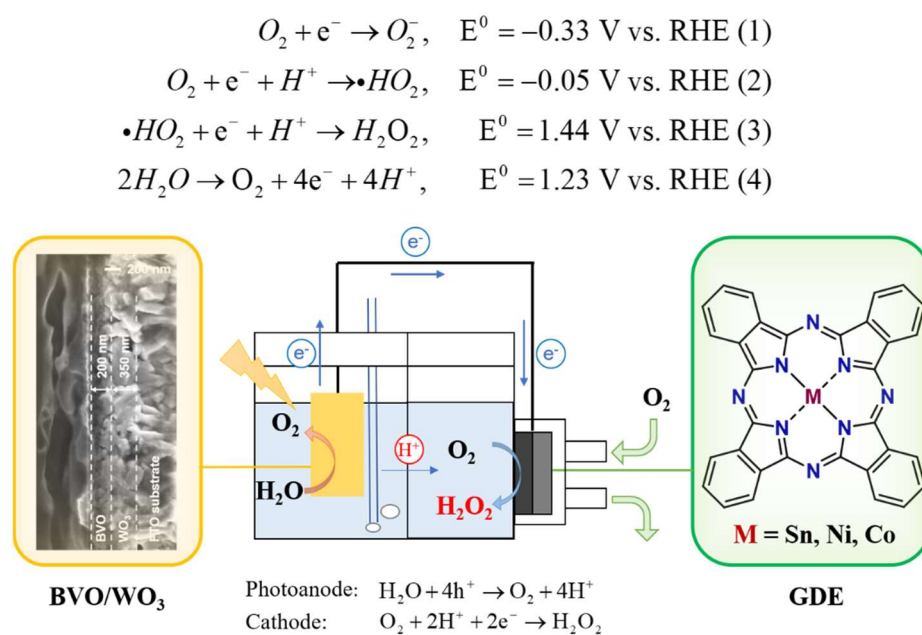
Hydrogen peroxide (H₂O₂) has been found widespread application in disinfection, bleaching, and chemical synthesis, making it one of the 100 most important chemical compounds in the world [1,2]. However, the traditional anthraquinone process for producing H₂O₂ is often associated with environmental challenges, such as high energy consumption and potential generation of hazardous by-products [3,4]. Photocatalytic synthesis provides an environmentally friendly and more energetically efficient alternative for producing H₂O₂. During this process, utilizing sunlight as a source of energy, only O₂ and H₂O are required to promote the synthesis of H₂O₂ under normal temperature and pressure conditions, resulting in a reduction of the dependence on fossil fuels and minimizing the environmental impact [5–8].

The conventional particle photocatalysts were limited by the rapid recombination of photogenerated carriers, resulting in a slow synthesis rate of H₂O₂ [9]. To address this issue, photoelectrocatalysis (PEC) systems were developed [10,11]. By adding an external applied bias, the photogenerated hole-electron pairs on the photoelectrode were effectively separated, thereby improving the H₂O₂ synthesis efficiency. A typical PEC cell usually contains a photoanode and a photocathode, with the anode and cathode chambers separated by a proton exchange membrane. The oxidation and reduction reactions take place in the photoanode and photocathode, respectively, offering greater selectivity to the reactions. Photocatalytic synthesis of H₂O₂ proceeds mainly through two pathways: water oxidation reaction (WOR) and oxygen reduction reaction (ORR) [4,10]. The WOR takes place on the photoanode, while the ORR occurs on the photocathode. For photoanodes, the primary materials used are metal oxides such as BVO [12–15], WO₃ [16,17], and TiO₂ [18,19]. Among these materials,

BVO is considered one of the most promising materials for fabricating photoanodes due to its suitable band gap (~2.4 eV) and excellent photo-corrosion stability [20,21]. However, its performance for WOR was constrained by limited electrical conductivity and carrier diffusion length, as well as slow water oxidation kinetics [22]. Therefore, surface modification of BVO, such as the creation of oxygen vacancies, is one of the key strategies to improve its PEC water oxidation activity [20,23]. On the other hand, studies on photocathodes are progressing at a slower pace, and a photocathodic material that possesses both high reaction efficiency and selectivity as well as high stability has yet to be identified.

A significant reason for the low rate of H₂O₂ synthesis on photocathodes is that ORR is a proton-coupled electron transfer process [3]. The solubility of O₂ in aqueous solutions is very low, limiting the mass transfer efficiency and leading to ineffective synthesis of the critical intermediate *OOH (−0.05 V vs. RHE; eq. 2), which results in a slow H₂O₂ production rate [24,25]. However, in the field of electrocatalysis, this problem has been effectively mitigated. A gas diffusion electrode (GDE), as a type of porous membrane electrode, facilitates the transport of a significant amount of gas to the interior of the electrode [26–29]. Upon contact with the electrolyte, a unique three-phase boundary system is formed. Utilizing this three-phase interface system can markedly enhance the rate of charge transfer from electrons to oxygen. Among the various GDEs, transition metal phthalocyanine (MPc) has been demonstrated to enhance ORR synthesis of H₂O₂ [30–33]. MPc was suitable as a material for the preparation of a GDE due to its low solubility in aqueous media and good thermal and chemical stability [32,34]. In addition, the catalytic performance of a GDE can be further optimized by changing the metal center of the phthalocyanine [30].

In this study, a modified BiVO₄ photoanode was utilized in conjunction with an MPc-modified GDE to overcome mass transfer issues in ORR and enhance the synthesis efficiency of H₂O₂ through a tandem electrode strategy (Scheme 1). Upon irradiation of the BVO photoanode with visible light, the excitation of hole-electron pairs initiated the OER by generating holes. The generated electrons were directed towards the SnPc-GDE for the reduction of O₂ to generate H₂O₂. Under conditions without external bias, the generation rate of H₂O₂ was measured at 952.5 μM·L^{−1}·h^{−1}, with a Faradaic efficiency of 48.4%.



Scheme 1. A tandem electrode strategy for the synthesis of H₂O₂.

2. Experimental

2.1. Chemicals

Unless otherwise stated, all of the chemicals used in the study were of analytical grade and used without further purification. All solutions were prepared by using ultra-pure water. WCl₆, Bi(NO₃)₃·5H₂O, VO(acac)₂, Na₂SO₃, N, N-dimethylformamide (DMF), Triton X-100, and acetic acid of analytical grade were purchased from Wako Pure Chemical Industries, Ltd., Japan. Ni mesh (100 mesh, 99.9% purity, 0.1 mm in thickness) was purchased from Nilaco Corporation, Japan. Hydrophobic carbon (HS-100) was purchased from Denki Kagaku Kogyo K.K, Japan. Hydrophilic carbon (ECP600JD) was purchased from Lion Corp., Japan.

2.2. Fabrication of a WO₃ Photoanode

The WO₃ photoelectrode was prepared on an F-doped SnO₂ conductive glass (FTO) substrate via spin coating. Typically, tungsten hexachloride (WCl₆) was dissolved in DMF, adjusted to a concentration of 504 mM, and subsequently applied to the FTO substrate by spin-coating (1000 rpm for 15 s), followed by calcination at 500 °C for 30 mins under an air atmosphere.

2.3. Fabrication of a BVO/WO₃ Photoanode

An acetic acid solution of 0.04 M Bi(NO₃)₃·5H₂O and an aqueous solution of 0.04 M VO(acac)₂ were stirred for 24 h, and then the two solutions were mixed and stirred for another 2 h. The mixture solution was spin-coated (1000 rpm, 10 s) onto an WO₃ underlayer and then baked at 500 °C for 30 mins in a muffle furnace under an air atmosphere. By repeating this spin-coating and calcination process 6 times, BVO/WO₃ electrodes were prepared in which BVO thickness was 200 nm.

2.4. Fabrication of an N-O_{vac}-BVO/WO₃ Photoanode

Oxygen vacancy-rich BVO (O_{vac}-BVO) photoanodes were prepared by the photoetching method. Typically, the BVO/WO₃ electrode was immersed in 0.5 M phosphate buffer solution containing 0.2 M Na₂SO₃ with a xenon lamp (AM 1.5) illumination for 10 mins. In order to further increase the oxygen vacancies on the surface, the BVO/WO₃ photoanode was calcined at 350 °C for 2 h under an N₂ atmosphere with a heating rate of 5 °C/min and an N₂ flow rate of 50 mL/min to obtain an N-O_{vac}-BVO/WO₃ photoanode.

2.5. GDE Preparation

A GDE was prepared from hydrophobic carbon, hydrophilic carbon and polytetrafluoroethylene (PTFE) by a molding process [35]. The GDE, consisting of a hydrophobic layer and a hydrophilic layer loaded with an MPc catalyst, was formed on an Ni mesh (Figure S1).

Hydrophobic carbon, surfactant (Triton X-100) and ultra-pure water were mixed in a ratio of 1:1:30 by weight for the preparation of hydrophobic powder. PTFE (67 wt% relative to carbon black) was added and then further mixed for 5 min. The prepared hydrophobic powder was frozen overnight then thawed and filtered. Subsequently, the pellets were dried at 120 °C for 12 h and then heat-treated at 300 °C for 3 h in air.

For preparation of hydrophilic powder, 36 wt% hydrophilic carbon and 32 wt% MPc catalyst were stirred in 100 mL ultra-pure water containing 1 mL butanol for 2 h. Subsequently 32 wt% PTFE was added and further stirred for 1 h. The suspension was filtered and then dried at 120 °C for 12 h.

2.6. Characterization of Catalysts

The crystalline phases were characterized by using a powder X-ray diffraction (XRD) instrument (MiniFlex II, Rigaku Co., Japan) with CuK α ($\lambda = 1.5418 \text{ \AA}$) radiation (cathode voltage: 30 kV, current: 15 mA). Scanning electron microscopy (SEM) images of BVO and WO₃ electrodes were obtained by a JEOL JSM-6701F field-emission scanning electron microscope. The absorption properties of the electrodes were measured using the diffuse reflection method with a UV-Vis spectrometer (UV-2600, Shimadzu Co., Japan) attached to an integral sphere at room temperature. X-ray photoelectron spectroscopy (XPS) measurements were performed by using a Kratos AXIS Nova spectrometer (Shimadzu Co., Japan) with a monochromatic Al K α X-ray source. The binding energy was calibrated by taking the C1s peak of contaminant carbon as a reference at 284.6 eV. The amount of H₂O₂ was determined by a colorimetric method using PACKTEST (WAK-H2O2, KYORITSU CHEMICAL-CHECK Lab., Corp., Japan) equipped with a digital PACKTEST spectrometer (ED723, GL Sciences Inc., USA).

3. Results and Discussion

3.1. Preparation and Characterization of N-O_{vac}-BVO/WO₃ Photoanode

Both the BVO layer and WO₃ layer were prepared via the spin-coating method [36,37]. The surface of the BVO electrode was modified by the photoetching method and subsequently annealed under an N₂ atmosphere to obtain the oxygen vacancy-enriched N-O_{vac}-BVO electrode. The WO₃ layer was composited with the BVO layer to establish a built-in electric field, thereby enhancing charge separation and improving the efficiency of OER. As shown in the SEM images, the WO₃ layer displayed a porous, loosely packed planar morphology with a thickness of approximately 350 nm (Figure 1a,c). The pores were filled after the BVO layer was coated with a thickness of *ca.* 200 nm and the surface of the electrode became smoother (Figure 1b,c). Generally, a smoother surface of the photoelectrode correlated with improved charge transfer, leading to more satisfactory activity [38]. XRD spectra was employed to confirm the physical phase components of the prepared materials. Typical diffraction peaks of WO₃ and BVO were observed in the XRD spectra (Figure 1d) and consistent with the reference patterns of WO₃ (JCPDS No. 43-1035) and BVO (JCPDS No. 14-0688), respectively, indicating the high purity of the prepared thin-film electrodes. The light absorption of BVO and BVO/WO₃ films prepared on FTO substrates was characterized by UV-Vis absorption spectroscopy. As illustrated in Figure 1e, the absorption edge of BVO was observed at approximately 510 nm, which was consistent with reported values [39]. After the modification of WO₃, the photoanode exhibited similar light absorption curves with a light absorption edge at 510 nm. Furthermore, an appreciable enhancement in light absorption was observed, which may contribute to enhanced photocatalytic activity.

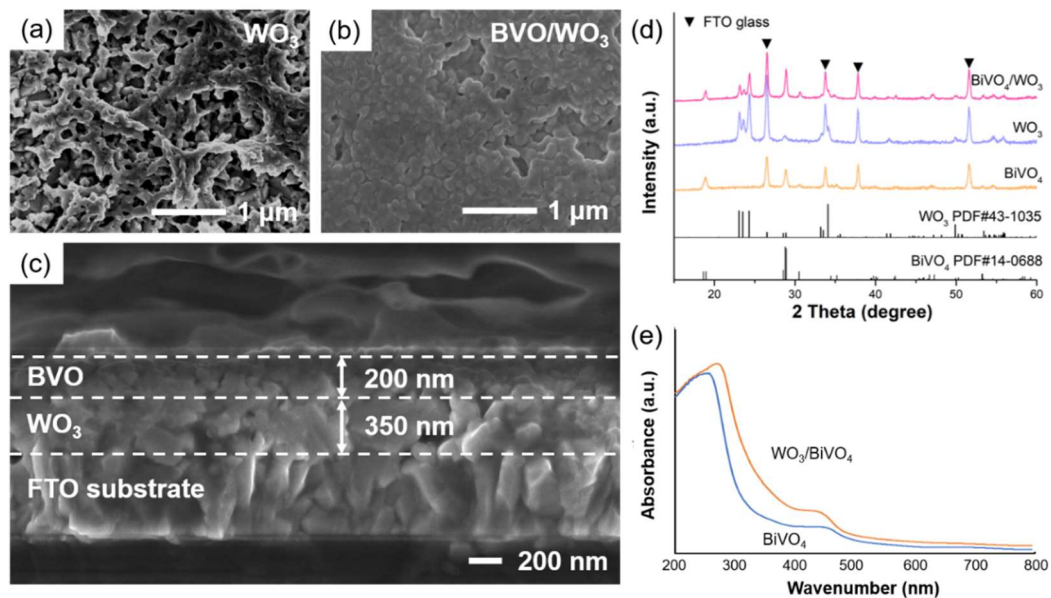


Figure 1. Top-view SEM images of (a) WO₃ and (b) WO₃/BVO photoanodes. (c) Cross-sectional SEM photograph of WO₃/BVO photoanode. (d) XRD analysis of WO₃, BVO, and WO₃/BVO photoanodes. (e) UV-Vis spectrum of WO₃/BVO photoanode.

The introduction of oxygen vacancies (O_v) has emerged as a highly effective approach to augment photocatalytic performance [24]. The impact of reported oxygen defects on the photocatalyst includes: 1. an increase in the carrier concentration; 2. promotion of separation and transmission of the carrier flow; 3. adjustment of the structure of energy regulation; 4. regulation of the adsorption and activation of molecular oxygen; 5. enhancement of optical absorption. In this study, inspired by a prior work [37], the construction of an oxygen-vacancy-enriched BiVO₄ (O_{vac}-BVO) photoanode was achieved by the photoetching method, and N-O_{vac}-BVO was obtained by further processing in an N₂ atmosphere for 2 h, which was confirmed by X-ray photoelectron spectroscopy (XPS) (Figure 2).

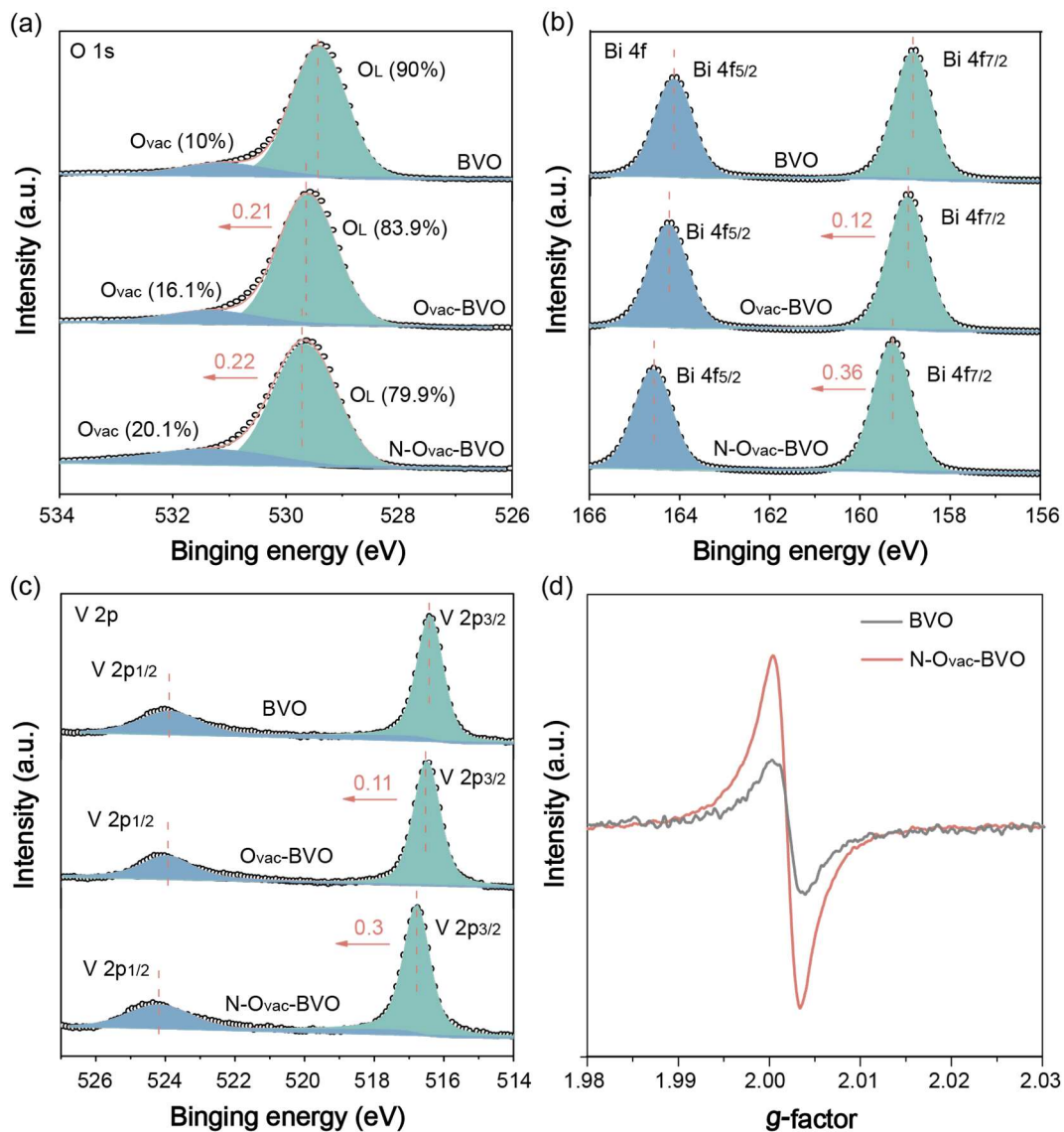


Figure 2. (a) O 1s, (b) Bi 4f, and (c) V 2p XPS spectra of BVO, N-O_{vac}-BVO and N-O_{vac}-BVO photoanodes. (d) EPR spectra of BVO and N-O_{vac}-BVO photoanodes.

In the XPS spectrum of O 1s, the peak corresponding to a lower binding energy (~ 529.4 eV) was assigned to the lattice oxygen (O_L^{2-}), while the peak with higher binding energy (~ 531.3 eV) was ascribed to O_{vac} [20]. After photoetching treatment, the relative abundance of O_{vac} increased from 10% to 16.1%. Following heating treatment in an N_2 atmosphere, the O_{vac} ratio further increased to 20.1%, proving that both photoetching treatment and heating treatment in an N_2 atmosphere could generate O_{vac} on the BVO electrode surface (Figure 2a). Compared with BVO, the Bi 4f, V 2p and O 1s peaks of O_{vac} -BVO and N- O_{vac} -BVO simultaneously shifted in the direction of high binding energy (Figure 2), which was consistent with the reported work [20,37]. The existence of O_{vac} was further proved by electron paramagnetic resonance (EPR) spectra. In the EPR spectrum of the N- O_{vac} -BVO photoanode, the signal corresponding to a g factor of 2.003 was significantly enhanced compared to that in the EPR spectrum of the BVO photoanode, which indicated a notable increase in the defect concentration of N- O_{vac} -BVO photoanode [37].

Figure 3a shows linear sweep voltammograms (LSVs) of WO_3 , BVO, O_{vac} -BVO, N- O_{vac} -BVO, and N- O_{vac} -BVO/ WO_3 photoanodes in CO_2 -bubbling 1.0 M $KHCO_3$ aqueous solution (1 M, pH = 7.5) under visible light illumination (420–800 nm, 100 mW/cm^2). The LSVs indicated that the abundant oxygen vacancies effectively improve the carrier separation efficiency. Notably, after a WO_3 layer modification, not only was the photocurrent of the N- O_{vac} -BVO/ WO_3 electrode improved, but the onset potential was also reduced from 0.57 V vs. RHE to 0.39 V vs. RHE. This may be attributed to the formation of the built-in electric field that promoted the transfer of electrons between the electrode surface and the electrolyte, thereby reducing the overpotential of the OER process. At a bias of 1.5 V_{RHE} , the current-time ($i-t$) curves for the aforementioned photoanodes were measured (Figure S3a). The experiments demonstrated that the N- O_{vac} -BVO/ WO_3 photoanode exhibited the highest photocurrent density, aligning with the trends

depicted in the J - V curves. Notably, all photoanodes displayed low Faradaic efficiencies for H_2O_2 synthesis (Figure S3b), indicating that the photogenerated carriers predominantly do not engage in the two-electron pathway for H_2O_2 formation but rather proceed via the four-electron pathway to effect O_2 evolution. This modality benefits by facilitating an increased electron transfer to the photocathode. Figure 3b shows the charge separation efficiency on the electrode surface with η_{surface} values of 35.6%, 39.7%, 69.4% and 82.2% for BVO, O_{vac} -BVO, N-O_{vac} -BVO, and N-O_{vac} -BVO/ WO_3 at 1.23 V vs. RHE, respectively.

Pt foil electrode was used as a reference to demonstrate the advantages of GDE in H_2O_2 synthesis. By adjusting the applied bias within the range from -0.5 to 1.5 V, it was found that the current density generated with SnPC-GDE cathode was significantly higher than that of the Pt foil electrode. Moreover, the generation rate of H_2O_2 was examined under the applied biases of -0.5 V and 1.5 V. After 3 hours testing, $2028.5 \mu\text{M}$ and $3404.4 \mu\text{M}$ of H_2O_2 were synthesized when SnPC-GDE cathode was used, which is approximately 13 times that of the Pt electrode under the same condition. Due to the unique three-phase interface of GDE, mass transfer between O_2 and the cathode is more efficient, thereby improving H_2O_2 generation rate [34].

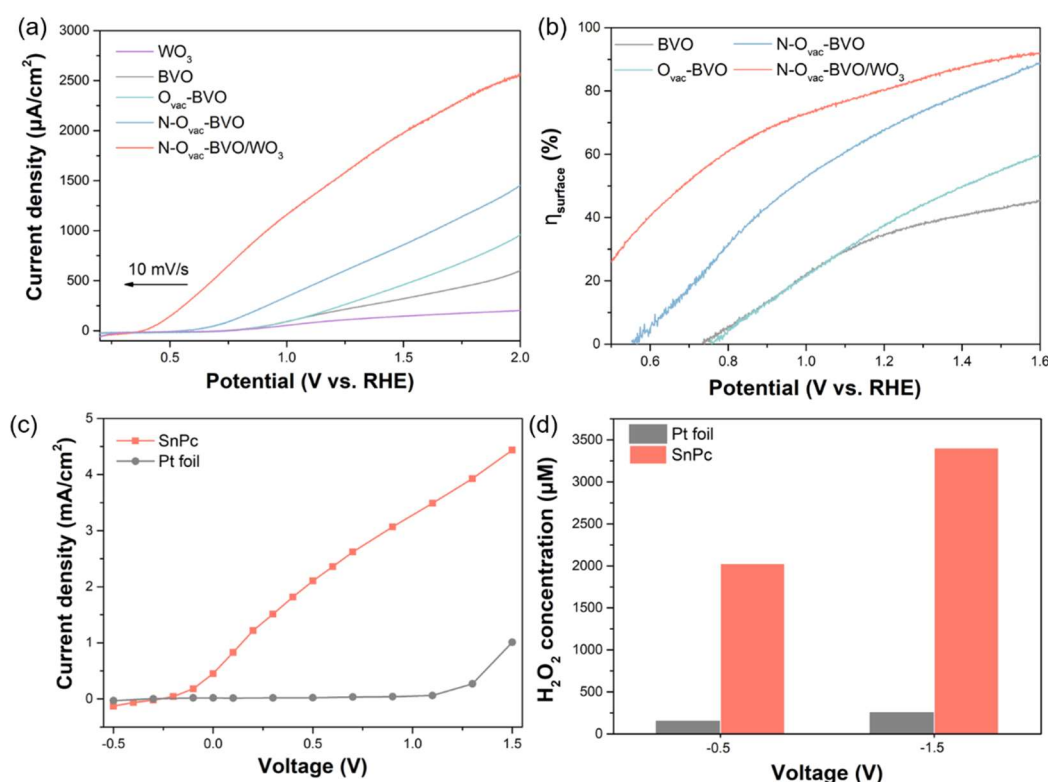


Figure 3. (a) J - V curves of WO_3 , BVO, O_{vac} -BVO, N-O_{vac} -BVO, and N-O_{vac} -BVO/ WO_3 photoanodes. (b) Charge separation efficiency on the surface (η_{surface}) of BVO, O_{vac} -BVO, N-O_{vac} -BVO, and N-O_{vac} -BVO/ WO_3 photoanodes. (c) Current density generated by SnPc-GDE and Pt foil in an air-bubbling phosphate buffer electrolyte (0.5 M , $\text{pH} = 6.5$) under different potential conditions with visible light irradiation ($420\text{--}800 \text{ nm}$, $100 \text{ mW}/\text{cm}^2$). (d) Amount of H_2O_2 generated by SnPc-GDE and Pt foil.

3.2. Effects of MPc Central Metal Cation (Ni, Co and Sn) on ORR

The GDE system effectively addressed the issue of limited O_2 solubility in aqueous solutions through its three-phase interfacial system, thus improving the efficiency of ORR. In the PEC system, the GDE was used as the working electrode, wherein the electrons transferred from the N-O_{vac} -BVO/ WO_3 photoanode were utilized for the reduction of O_2 , thereby facilitating the synthesis of H_2O_2 (Figure S2). Figure 4a illustrated the voltage distribution of the N-O_{vac} -BVO/ WO_3 photoanode and SnPc-GDE under illumination and different applied biases from 0.5 V to -1.5 V (GDE vs N-O_{vac} -BVO/ WO_3). At 0.44 V vs. RHE, the convergence of the two curves indicated that no external bias was applied between the N-O_{vac} -BVO/ WO_3 photoanode and the SnPc-GDE under these conditions.

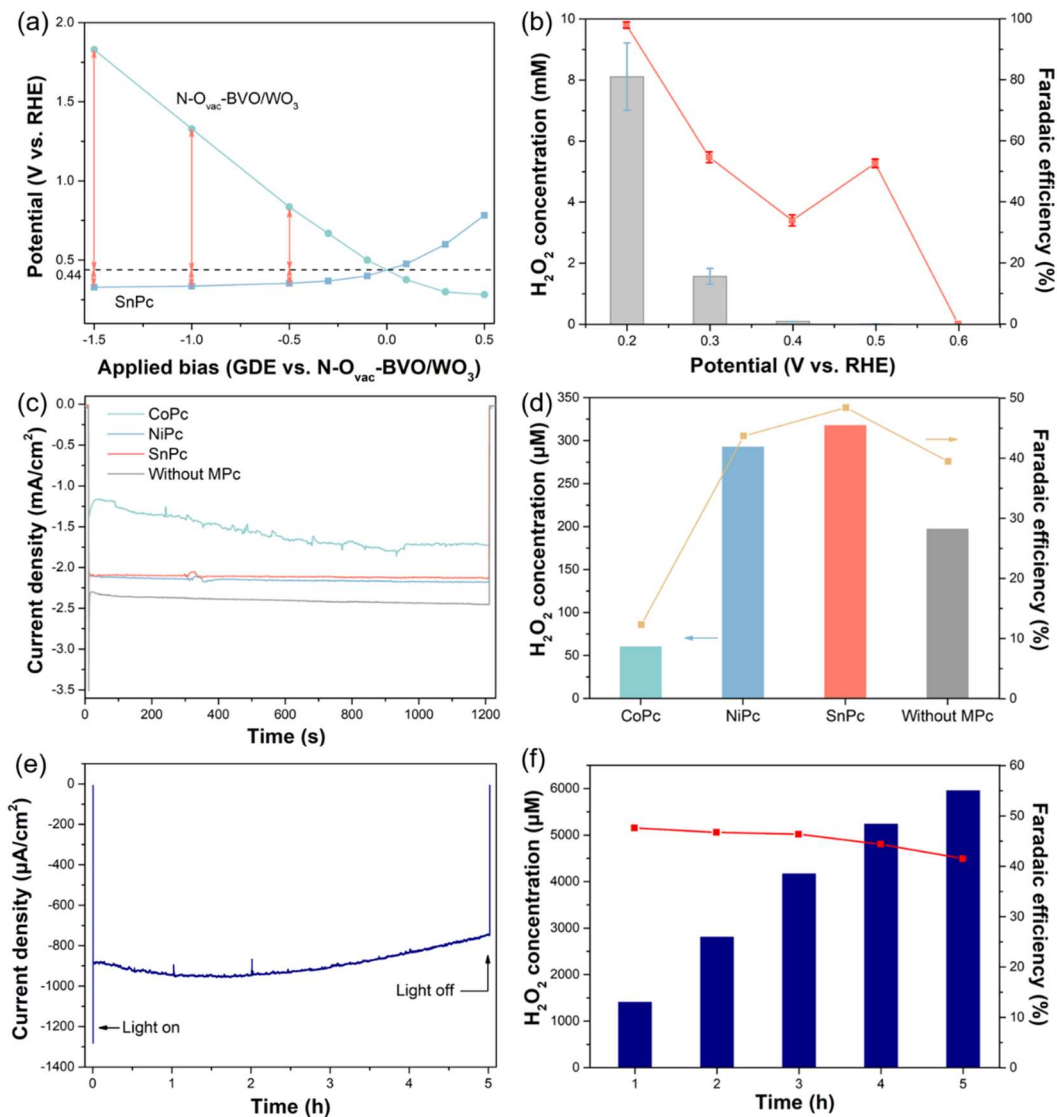


Figure 4. (a) Distribution of applied bias on N-O_{vac}-BVO/WO₃ and SnPc-GDE. (b) Amount of H₂O₂ generated by SnPc-GDE in an air-bubbling phosphate buffer electrolyte (0.5 M, pH = 6.5) under different potential conditions with visible light irradiation (420–800 nm, 100 mW/cm²). (c) *i-t* curves of CoPc, NiPc, SnPc and without MPc GDE cathodes under a potentiostatic condition at +0.44 V_{RHE}. (d) Amount of H₂O₂ generated by the CoPc, NiPc, SnPc and without MPc GDE cathodes and corresponding Faraday efficiency values. (e) Five-hour stability test of the SnPc GDE cathode. (f) Amount of H₂O₂ generated by the SnPc GDE cathode and corresponding Faraday efficiency.

Inexpensive transition metals (Co, Ni, and Sn) are used as coordination centers for phthalocyanine. Transition metal atoms typically have incompletely filled d-orbitals, which enables them to form strong chemical bonds with reaction intermediates such as *O₂⁻, *OOH, and *OH, thus providing effective active sites [40]. Different transition metal elements have different electronic configurations, oxidation states and coordination properties, which directly affect the catalytic performance of MPc [32]. The activity and selectivity of phthalocyanine GDEs modified with Co, Ni, and Sn for ORR were compared under 0.44 V vs. RHE (Figure 4c). Through the *i-t* curves, it was found that the SnPc electrode has good stability, and the generation rate of H₂O₂ reached 952.5 μM·L⁻¹·h⁻¹, corresponding to a Faradaic efficiency of 48.4%. The reason Sn acts as a better active center may be due to the fact that SnN₄ only requires a dissociation energy of 0.63 eV to break the O-O bond [41]. The amount of H₂O₂ generation reached ca. 16288.3 μM·L⁻¹·h⁻¹ with a corresponding Faradaic efficiency of 97.9% under the potential of 0.2 V_{RHE}, indicating that the current applied by the potentiostat was involved in ORR (Figure 4b and Figure S4). To further test the stability of the electrodes, a prolonged reaction was performed. After 5 hours of reaction, the photocurrent decreased slightly, while the Faradaic efficiency remained stable (Figure 4e,f).

4. Conclusions

In this work, a modified BiVO₄ photoanode combined with an SnPc-GDE was utilized for the synthesis of H₂O₂. When visible light was irradiated on the BVO photoanode, the hole-electron pairs were excited and the OER was driven through the holes, and the excited electrons were transferred to the SnPc-GDE to reduce O₂ for the synthesis of H₂O₂. Increase in oxygen vacancy was achieved by photoetching the BVO electrode, followed by annealing in an N₂ atmosphere, culminating in the formation of the N-O_{vac}-BVO electrode. The enriched oxygen vacancies effectively promoted electron-hole pair separation and enhanced the charge separation efficiency on the electrode surface. The N-O_{vac}-BVO electrode was combined with WO₃ to form a built-in electric field, which further promoted charge separation and reduced the onset potential of OER. The SnPc catalyst-modified GDE electrode demonstrated superior selectivity for ORR and maintained its stability throughout prolonged reaction cycles. Under unbiased conditions, the H₂O₂ production rate reached 952.5 μM·L⁻¹·h⁻¹ accompanied by a Faradaic efficiency of 48.4%.

Supplementary Materials

Summarize the supplementary information with the caption names in this section. The following supporting information can be found at: <https://www.sciepublish.com/article/pii/177>, Fig. S1: Photos of (a) WO₃/BVO photoanode and (b) SnPc-GDE. (c) Schematic diagram of the structure of GDE. The bottom layer is the Ni network, the middle is the hydrophobic layer, and the top layer is the hydrophilic layer; Fig. S2: (a) Photo of the PEC system. (b) Schematic diagram of the PEC system; Fig. S3: (a) CA curves of WO₃, BVO, O_{vac}-BVO, N-O_{vac}-BVO, and N-O_{vac}-BVO/WO₃ photoanodes under the potential of 1.5 V_{RHE}. (b) Amount of H₂O₂ generated by WO₃, BVO, O_{vac}-BVO, N-O_{vac}-BVO, and N-O_{vac}-BVO/WO₃ photoanodes in a CO₂-bubbling KHCO₃ electrolyte (1 M, pH = 7.6) under the potential of 1.5 V_{RHE} with visible light irradiation (420–800 nm, 100 mW/cm²) and Pt electrode as a counter electrode; Fig. S4: Time courses of the photocurrents of SnPc-GDE in an air-bubbling phosphate buffer electrolyte (0.5 M, pH = 6.5) under different potential conditions with visible light irradiation (420–800 nm, 100 mW/cm²). Potential conditions: (a) 0.2 V vs. RHE, (b) 0.3 V vs. RHE, (c) 0.3 V vs. RHE and (d) 0.5 V vs. RHE; Table S1: Comparison of different photocathodes for H₂O₂ producing with current study.

Author Contributions

Conceptualization, C.C. and T.O.; Methodology, N.T.; Software, N.T.; Validation, N.T., C.C. and W.C.; Formal Analysis, C.C.; Investigation, N.T.; Resources, N.T.; Data Curation, N.Y.; Writing – Original Draft Preparation, C.C.; Writing – Review & Editing, Q.Z.; Visualization, C.C. and N.T.; Supervision, T.O.; Project Administration, T.O.; Funding Acquisition, T.O. and Q.Z.

Ethics Statement

Not applicable.

Informed Consent Statement

Not applicable.

Funding

This work was funded by the Guangdong Basic and Applied Basic Research Foundation (Grant Nos. 2024A1515010976 and 2020A1515010982) and Japan Society for the Promotion of Science (JSPS), Grant-in-Aid for Scientific Research (B) (20H02847).

Declaration of Competing Interest

The authors declare that they have no known competing financial interests or personal relationships that could have appeared to influence the work reported in this paper.

References

1. Myers RL. The 100 most important chemical compounds: A reference guide. *J. Chem. Educ.* **2009**, *86*, 1182.
2. Chen Z, Yao D, Chu C, Mao S. Photocatalytic H₂O₂ production systems: Design strategies and environmental applications. *Chem. Eng. J.* **2023**, *451*, 138489.

3. Teng Z, Zhang Q, Yang H, Kato K, Yang W, Lu Y-R, et al. Atomically dispersed antimony on carbon nitride for the artificial photosynthesis of hydrogen peroxide. *Nat. Catal.* **2021**, *4*, 374–384.
4. Qu S, Wu H, Ng YH. Clean production of hydrogen peroxide: A heterogeneous solar-driven redox process. *Adv. Energy Mater.* **2023**, *13*, 2301047.
5. Zhang Y, Cao Q, Meng A, Wu X, Xiao Y, Su C, et al. Molecular heptazine-triazine junction over carbon nitride frameworks for artificial photosynthesis of hydrogen peroxide. *Adv. Mater.* **2023**, *35*, e2306831.
6. He K, Huang Z, Chen C, Qiu C, Zhong YL, Zhang Q. Exploring the roles of single atom in hydrogen peroxide photosynthesis. *Nano-Micro Lett.* **2024**, *16*, 23.
7. Yu FY, Zhou YJ, Tan HQ, Li YG, Kang ZH. Versatile photoelectrocatalysis strategy raising up the green production of hydrogen peroxide. *Adv. Energy Mater.* **2023**, *13*, 2300119.
8. Zeng X, Liu Y, Hu X, Zhang X. Photoredox catalysis over semiconductors for light-driven hydrogen peroxide production. *Green Chem.* **2021**, *23*, 1466–1494.
9. Xie Y, Zhang Q, Sun H, Teng Z, Su C. Semiconducting polymers for photosynthesis of H₂O₂: Spatial separation and synergistic utilization of photoredox centers. *Acta Phys. Chim. Sin.* **2023**, *39*, 2301001.
10. Sun Y, Han L, Strasser P. A comparative perspective of electrochemical and photochemical approaches for catalytic H₂O₂ production. *Chem. Soc. Rev.* **2020**, *49*, 6605–6631.
11. Wu H, Tan HL, Toe CY, Scott J, Wang L, Amal R, Ng YH. Photocatalytic and photoelectrochemical systems: similarities and differences. *Adv. Mater.* **2020**, *32*, 1904717.
12. Fuku K, Sayama K. Efficient oxidative hydrogen peroxide production and accumulation in photoelectrochemical water splitting using a tungsten trioxide/bismuth vanadate photoanode. *Chem. Commun.* **2016**, *52*, 5406–5409.
13. Hou H, Zeng X, Zhang X. Production of hydrogen peroxide by photocatalytic processes. *Angew. Chem. Int. Ed.* **2020**, *59*, 17356–17376.
14. Guo ML, Wan SP, Li CL, Zhang K. Graphene oxide as a hole extraction layer loaded on BiVO₄ photoanode for highly efficient photoelectrochemical water splitting. *Rare Metals* **2022**, *41*, 3795–3802.
15. Wu X, Ling Tan H, Zhang C, Teng Z, Liu Z, Hau Ng Y, et al. Recent advances in two-dimensional ultrathin Bi-based photocatalysts. *Progr. Mater. Sci.* **2023**, *133*, 101047.
16. Bai L, Jia S, Gao Y, Li C, Chen X, Zhou S, et al. A p-n WO₃/SnSe₂ heterojunction for efficient photo-assisted electrocatalysis of the oxygen evolution reaction. *Energy Environ. Mater.* **2023**, *6*, e12456.
17. Jamila GS, Sajjad S, Leghari SAK, Long M. Nitrogen doped carbon quantum dots and GO modified WO₃ nanosheets combination as an effective visible photo catalyst. *J. Hazard. Mater.* **2020**, *382*, 121087.
18. Sun LJ, Su HW, Liu QQ, Hu J, Wang LL, Tang H. A review on photocatalytic systems capable of synchronously utilizing photogenerated electrons and holes. *Rare Metals* **2022**, *41*, 2387–2404.
19. Zheng L, Teng F, Ye X, Zheng H, Fang, X. Photo/electrochemical applications of metal sulfide/TiO₂ heterostructures. *Adv. Energy Mater.* **2019**, *10*, 1902355.
20. Feng S, Wang T, Liu B, Hu C, Li L, Zhao ZJ, Gong J. Enriched surface oxygen vacancies of photoanodes by photoetching with enhanced charge separation. *Angew. Chem. Int. Ed.* **2019**, *59*, 2044–2048.
21. Zhong X, He H, Yang M, Ke G, Zhao Z, Dong F, et al. In³⁺-doped BiVO₄ photoanodes with passivated surface states for photoelectrochemical water oxidation. *J. Mater. Chem. A* **2018**, *6*, 10456–10465.
22. Kim TW, Choi KS. Nanoporous BiVO₄ photoanodes with dual-layer oxygen evolution catalysts for solar water splitting. *Science* **2014**, *343*, 990–994.
23. Fuku K, Miyase Y, Miseki Y, Funaki T, Gunji T, Sayama K. Photoelectrochemical hydrogen peroxide production from water on a WO₃/BiVO₄ photoanode and from O₂ on an Au cathode without external bias. *Chem. Asian J.* **2017**, *12*, 1111–1119.
24. Ji Q, Bi L, Zhang J, Cao H, Zhao XS. The role of oxygen vacancies of ABO₃ perovskite oxides in the oxygen reduction reaction. *Energy Environ. Sci.* **2020**, *13*, 1408–1428.
25. Li L, Wang P, Shao Q, Huang X. Recent progress in advanced electrocatalyst design for acidic oxygen evolution reaction. *Adv. Mater.* **2021**, *33*, 4243.
26. Nguyen TN, Dinh CT. Gas diffusion electrode design for electrochemical carbon dioxide reduction. *Chem. Soc. Rev.* **2020**, *49*, 7488–7504.
27. Santos GOS, Cordeiro-Junior PJM, Sánchez-Montes I, Souto RS, Kronka MS, Lanza, MRV. Recent advances in H₂O₂ electrosynthesis based on the application of gas diffusion electrodes: Challenges and opportunities. *Curr. Opin. Electrochem.* **2022**, *36*, 101124.
28. Zhang Y, Mascaretti L, Melchionna M, Henrotte O, Kment Š, Fornasiero P, Naldoni A. Thermoplasmonic in situ fabrication of nanohybrid electrocatalysts over gas diffusion electrodes for enhanced H₂O₂ electrosynthesis. *ACS Catal.* **2023**, *13*, 10205–10216.
29. Wang J, Li C, Rauf M, Wang W. Highly efficient H₂O₂ electrogeneration enabled by controlling the wettability of gas diffusion electrodes and the reaction pathway in divided cells. *ACS Sustain. Chem. Eng.* **2022**, *11*, 436–443.
30. Guo X, Lin S, Gu J, Zhang S, Chen Z, Huang S. Simultaneously achieving high activity and selectivity toward two-electron O₂ electroreduction: The power of single-atom catalysts. *ACS Catal.* **2019**, *9*, 11042–11054.

31. Silva FL, Reis RM, Barros WRP, Rocha RS, Lanza MRV. Electrogeneration of hydrogen peroxide in gas diffusion electrodes: Application of iron (II) phthalocyanine as a modifier of carbon black. *J. Electroanal. Chem.* **2014**, *722*, 32–37.
32. Wu Y, Liang Y, Wang H. Heterogeneous molecular catalysts of metal phthalocyanines for electrochemical CO₂ reduction reactions. *Acc. Chem. Res.* **2021**, *54*, 3149–3159.
33. Morishige STK, Iwano G. Adsorption of CO, O₂, NO₂, and NH₃ by metallophthalocyanine monolayers supported on graphite. *Langmuir* **1997**, *13*, 5184–5188.
34. Barros WRP, Reis RM, Rocha RS, Lanza MRV. Electrogeneration of hydrogen peroxide in acidic medium using gas diffusion electrodes modified with cobalt (II) phthalocyanine. *Electrochim. Acta* **2013**, *104*, 12–18.
35. Kobayashi K, Lou SN, Takatsuji Y, Haruyama T, Shimizu Y, Ohno T. Photoelectrochemical reduction of CO₂ using a TiO₂ photoanode and a gas diffusion electrode modified with a metal phthalocyanine catalyst. *Electrochim. Acta* **2020**, *338*, 135805.
36. Fuku K, Miyase Y, Miseki Y, Gunji T, Sayama K. WO₃/BiVO₄ photoanode coated with mesoporous Al₂O₃ layer for oxidative production of hydrogen peroxide from water with high selectivity. *RSC Adv.* **2017**, *7*, 47619–47623.
37. Wan S, Dong C, Jin J, Li J, Zhong Q, Zhang K, et al. Tuning the surface wettability of a BiVO₄ photoanode for kinetically modulating water oxidative H₂O₂ accumulation. *ACS Energy Lett.* **2022**, *7*, 3024–3031.
38. Chen C, Yasugi M, Yu L, Teng Z, Ohno T. Visible light-driven H₂O₂ synthesis by a Cu₃BiS₃ photocathode via a photoelectrochemical indirect two-electron oxygen reduction reaction. *Appl. Catal. B Environ.* **2022**, *307*, 121152.
39. Liu C, Mao S, Shi M, Hong X, Wang D, Wang F, et al. Enhanced photocatalytic degradation performance of BiVO₄/BiOBr through combining Fermi level alteration and oxygen defect engineering. *Chem. Eng. J.* **2022**, *449*, 137757.
40. Guo X, Lin S, Gu J, Zhang S, Chen Z, Huang S. Simultaneously achieving high activity and selectivity toward two-electron O₂ electroreduction: the power of single-atom catalysts. *ACS Catal.* **2019**, *9*, 11042–11054.
41. Chen Y, Sun F, Tang Q. The active structure of p-block SnNC single-atom electrocatalysts for the oxygen reduction reaction. *Phys. Chem. Chem. Phys.* **2022**, *24*, 27302–27311.